

N -body Models of Rotating Globular Clusters

A. Ernst^{1,2*}, P. Glaschke^{1,2}, J. Fiestas¹, A. Just¹ and R. Spurzem^{1†}

¹*Astronomisches Rechen-Institut / Zentr. Astron. Univ. Heidelberg, Mönchhofstr. 12-14, 69120 Heidelberg, Germany*

²*Max-Planck-Institut für Astronomie, Königstuhl 17, 69117 Heidelberg, Germany*

Accepted ... Received ...

ABSTRACT

We have studied the dynamical evolution of rotating globular clusters with direct N -body models. Our initial models are rotating King models; we obtained results for both equal-mass systems and systems composed out of two mass components. Previous investigations using a Fokker-Planck solver have revealed that rotation has a noticeable influence on stellar systems like globular clusters, which evolve by two-body relaxation. In particular, it accelerates their dynamical evolution through the gravogyro instability. We have validated the occurrence of the gravogyro instability with direct N -body models. In the case of systems composed out of two mass components, mass segregation takes place, which competes with the rotation in the acceleration of the core collapse. The “accelerating” effect of rotation has not been detected in our isolated two-mass N -body models. Last, but not least, we have looked at rotating N -body models in a tidal field within the tidal approximation. It turns out that rotation increases the escape rate significantly. A difference between retrograde and prograde rotating star clusters occurs with respect to the orbit of the star cluster around the Galaxy, which is due to the presence of a “third integral” and chaotic scattering, respectively.

Key words: N -body simulations – rotating star clusters.

1 INTRODUCTION

This paper is devoted to an intriguing problem in the dynamics of globular clusters: How an overall rotation of a globular cluster affects its dynamical evolution. There is a wealth of observational data which indicates that typical globular clusters are rotating. The first method for the detection of rotation in globular clusters dates back in the first half of 20th century. Observations showed that “flattening” (i.e. a deviation of spherical symmetry) is a common feature of globular clusters. The first ellipticity measurements have been done by H. Shapley in the 1920s, see Shapley (1930). Subsequent ellipticity measurements of Galactic and extragalactic globular clusters have been done, among others, by Geisler & Hodge (1980), Frenk & Fall (1982), Geyer et al. (1983), White & Shawl (1987), Staneva, Spassova & Golev (1996). The ellipticities of Galactic globular clusters are now given in the Harris catalogue,¹ cf. Harris (1996). A second method for the detection of rotation of globular clusters relies on radial velocity measurements of individual stars in globulars (Wilson & Coffeen 1954, Mayor et al.

1984, Meylan & Mayor 1986, Gebhardt et al. 1994, 1995, 2000, Reijns et al. 2006 and references therein). The measured radial velocities can be plotted against the position angle. The amplitude of a sine curve which is fitted through the data points serves as a rough measure (i.e. a lower limit) for the degree of rotation of the star cluster. Proper motions of individual stars have been measured as well and used for the detection of rotation in globular clusters (e.g. Peterson & Cudworth 1994, van Leeuwen et al. 2000 or Anderson & King 2003. The authors of the latter two references conclude for ω Cen and 47 Tuc that their axes of rotation are considerably inclined to the plane of the sky). Table 7.2 in the review by Meylan & Heggie (1997) gives already an overview of the degrees of rotation of Galactic globular clusters. For instance, Gebhardt et al. (1995) estimated $V_{\text{rot}}/\sigma_{1D} \simeq 0.2$ for the evolved clusters M15 and 47 Tuc. However, globular clusters in the Large and Small Magellanic Clouds are younger and markedly more elliptical than typical Galactic globulars (see the above references), which suggests higher values of $V_{\text{rot}}/\sigma_{1D}$.

From the theoretical side, the first published study of a rotating system of $N = 100$ bodies is the work by Aarseth (1969) which aimed at the dynamical evolution of clusters of galaxies. He already detected a flattening caused by rotation. Subsequent attempts to study rotating globular clus-

* email: aernst@ari.uni-heidelberg.de

† email: spurzem@ari.uni-heidelberg.de

¹ <http://physwww.physics.mcmaster.ca/harris/mwgc.dat>

ters with direct N -body models have been made by Wielen (1974) for systems with particle numbers $N = 50 - 250$ and Akiyama & Sugimoto (1989) for $N = 1000$. Wielen concludes that “a slow overall rotation of a globular cluster does not significantly affect the dynamical evolution”, and Akiyama & Sugimoto do not yet clearly demonstrate numerically the existence of the gravogyro instability (see below) “because of statistical noise due to a small number of particles”. More recent numerical studies of rotating globular clusters have been done using the Fokker-Planck [hereafter: FP] method, see the PhD thesis of Einsel (1996), Einsel & Spurzem (1999) [hereafter ES99], the follow-up papers by Kim et al. (2002, 2004) and the PhD thesis of Kim (2003) [hereafter K02, K03, K04]. Under certain approximations, the evolution of a phase space distribution function which describes the macroscopic state of a globular cluster, is followed by the numerical solution of the FP equation. The advantage of such approximate models is their computational speed, i.e. one can do large parameter studies in a reasonable time. For the most recent FP models including rotation, which are compared directly to observations of M5, M15, 47 Tuc and ω Cen, see Fiestas et al. (2006).²

The present study is again concerned with N -body models of rotating globular clusters. Based on Newton’s law of gravitation, N -body modelling is probably the most direct way to investigate the dynamics of stars in globular clusters. However, it is computationally expensive and time-consuming.³ On the other hand, direct N -body modelling particularly allows to test the validity of assumptions used in statistical modelling of globular clusters, like FP models.

This paper is organized as follows: Section 2 describes our initial models and the numerical method. In Section 3 we will have a closer look at the effect of rotation on the core collapse in isolated equal-mass models. It is well-known that the core collapse is caused by the gravothermal instability: The negative heat capacity of the self-gravitating core of the star cluster leads to an amplification of temperature gradients if the halo of the star cluster is extensive enough. The core collapse is stopped by the formation of a few binaries in the core of the star cluster by three-body processes (Giersz & Heggie 1994b, 1996). These produce heat at a rate slightly higher than the rate of energy loss due to two-body relaxation, thereby cooling the cluster core which has negative heat capacity. If the star cluster rotates, we numerically demonstrate in Section 3 that an additional instability occurs: The gravogyro instability, which accelerates the core collapse in our equal-mass models. In Section 4, which is dedicated to tidally limited models, we additionally study the escape of stars from rotating star clusters, i.e. mass loss⁴

across the tidal boundary. In Section 5, which treats rotating systems composed out of two mass components, we study the interplay between rotation and mass segregation.

2 INITIAL MODELS / NUMERICAL METHOD

We employ generalized King models with rotation. The distribution function is given by

$$f(E, J_z) = C \cdot \left[\exp\left(-\frac{E - \Phi_t}{\sigma_K^2}\right) - 1 \right] \cdot \exp\left(-\frac{\Omega_0 J_z}{\sigma_K^2}\right), \quad (1)$$

which depends on the integrals of motion E (energy) and J_z (z -component of angular momentum), where Φ_t is the potential at the outer boundary of the model (i.e. at the radius where the density approaches zero), σ_K is the King velocity dispersion (which is not the central velocity dispersion) and Ω_0 is close to the angular speed in the cluster center (which has nearly solid body rotation). In the distribution function (1), the first two factors on the right-hand side represent just a usual King model. The last factor, which depends on J_z , introduces rotation into the model, i.e. a difference between positive and negative J_z . It also allows for anisotropy, i.e. we have $\sigma_r = \sigma_z \neq \sigma_\phi$ for the velocity dispersions in radial, vertical and tangential directions, respectively. Note that models where $f \propto \exp(-\gamma J_z)$ have been first used by Prendergast & Toomer (1970) and Wilson (1975) to model elliptical galaxies. However, this term in combination with a King model has been first used in Goodman (1983, unpublished), then by Lagoute & Longaretti (1996), Longaretti & Lagoute (1996), Einsel (1996), ES99, K02, K03 and K04, Fiestas (2006) and Fiestas et al. (2006).

The rotating King model based on the distribution function (1) possesses rotational symmetry and differential rotation. It has two dimensionless free parameters: The King parameter $W_0 = -(\Phi_0 - \Phi_t)/\sigma_K^2$, where Φ_0 is the central potential, and the rotation parameter $\omega_0 = \sqrt{9/(4\pi G \rho_c)} \cdot \Omega_0$, where G is the gravitational constant and ρ_c is the central density. It reduces to a King model in the limit $\omega_0 = 0$. ES99 give the ratio $\lambda = T_{\text{rot}}/T_{\text{kin}}$ of rotational to kinetic energy in percent in their Table 1 for rotating King models with $W_0 = 6$. The ratio of the root mean squared rotational velocity to the velocity dispersion is then given by $V_{\text{rot}}/\sigma_{1D} = \sqrt{3\lambda/(1-\lambda)}$, which may be compared with observations. Furthermore, it may be of interest to note that between $0.7 < \omega_0 < 0.8$ there is a transition where the initial axisymmetric isolated rotating King models become unstable to the formation of a bar (P. Berczik, priv. comm.).

Our models composed out of two mass components are initially uniformly mixed and characterized by two additional dimensionless parameters, the stellar mass ratio $\mu = m_2/m_1$, where m_1 and m_2 are the individual masses of the light and heavy stars, respectively, and the mass fraction of heavy stars $q = M_2/M$, where M_2 is the total mass of the heavy component and M is the total mass of the star cluster.

In direct N -body models, the main constraint for a reasonable computing time is the number of particles N . In our simulations, we use $N = 5000$ for all models with $\mu \leq 10$ (including all equal-mass models) and $N = 32000$ for models with $\mu = 25$ and $\mu = 50$. A typical simulation for one of

² A database of rotating star cluster models exists at the ARI: <http://www.ari.uni-heidelberg.de/clusterdata/>

³ Therefore N -body codes for massively parallel computers have been written. Moreover, special-purpose hardware systems like GRAPE boards have been in use for N -body simulations since the early 1990s (see <http://grape.astron.s.u-tokyo.ac.jp/grape/>). A new development is a technology based on FPGAs (Field Programmable Gate Arrays). However, such hardware is not used in the present study.

⁴ The term “mass loss” is not used in the usual sense (due to stellar evolution), but in the sense of a mass loss of the whole star cluster through escaping stars (i.e. due to dynamical interactions).

our equal-mass models took about three days on a 3 GHz Pentium PC, until the core collapse time was reached.

The codes used are NBODY6++ (e.g. Spurzem 1999) and NBODY6 (see Aarseth 1999, 2003 for an overview). The former code is a variant of the latter modified in order to run on massively parallel computers. Both codes share, aside from parallelization, the same fundamental features and yield comparable results. A fourth-order Hermite scheme, applied first by Makino & Aarseth (1992), is used for the direct integration of the Newtonian equations of motion of the N -body system. The codes use adaptive and individual time steps, which are organized in hierarchical block time steps, the Ahmad-Cohen neighbor scheme (Ahmad & Cohen 1973), Kustaanheimo-Stiefel regularization of close encounters (Kustaanheimo & Stiefel 1965) and Chain regularization (Mikkola & Aarseth 1990, 1993, 1996, 1998).

All models done with NBODY6++ have been calculated on single-processor machines at the ARI, except the two-mass models TM9-TM12 (see section 5). Some models (from series EM2, see Section 3) have been calculated using Aarseth's original code NBODY6. For some models, we used averaging over several runs with the same particle number N but different initial values for positions and velocities. This was done in order to obtain a better statistical quality, cf. Section 2.2 of Giersz & Heggie (1994a) for a discussion of this approach. Averaging increases the computing time for gravitational forces of a system of N bodies on a linear scale, whereas increasing the particle number N increases the computing time for gravitational forces $\propto N^2$ in the limit of high N . Since we consider in the present work processes acting on the relaxation time scale, an extra power of N contributes to the scaling of the total computing time of a model. In our averaged models, the physical quantities shown in the plots are determined as the arithmetic mean of those values of the considered quantity, which resulted from the individual runs.

The quantities on the vertical axis of our figures are shown in dimensionless N -body units, i.e. $G = M = -4E = 1$, where G is the gravitational constant, M is the total mass of the system and E the total energy, see Heggie & Mathieu (1986). The resulting length unit is the virial radius $r_V = GM^2/(-4E)$, which is of the order of the half-mass radius of a globular cluster, see, for instance, Table 1 in Gürkan et al. (2004). The resulting time unit is then given by $t_V = (GM/r_V^3)^{-1/2}$. The time on the horizontal axis of most figures is shown in units of the initial half-mass relaxation time, i.e. the t_{rh} means $t_{rh}(0)$. For the half-mass relaxation time, we adopted the expression

$$t_{rh} = \frac{8\pi}{3} \frac{[\sqrt{2|E|/M} r_V]^3 N}{15.4 G^2 M^2 \ln(\gamma N)}. \quad (2)$$

with $\gamma = 0.11$. The above definition is based on Equation (5) of the paper by Spitzer & Hart (1971) with

$$n = \frac{3N}{8\pi r_V^3}, \quad v_m = \sqrt{\frac{2|E|}{M}}, \quad m = \frac{M}{N} \quad (3)$$

for the mean value of the particle density inside r_V , the root mean squared stellar velocity (i.e. the 3D velocity disper-

Model	W_0	ω_0	N	Averaging	t_{cc}/t_{rh}
EM1a	3	0.0	5K	no	10.68
EM1b	3	0.3	5K	no	10.10
EM1c	3	0.6	5K	no	10.35
EM2a	6	0.0	5K	4	7.51 ± 0.52
EM2b	6	0.3	5K	4	7.45 ± 0.25
EM2c	6	0.6	5K	4	7.03 ± 0.19
EM2d	6	0.9	5K	3	6.19 ± 0.35

Table 1. The initial isolated equal-mass models. For the models of series EM2 we also give the run-to-run variation σ_{n-1} in t_{cc}/t_{rh} in the last column.

sion) and the mean stellar mass, respectively. It may be of interest to note that (2) can be written in terms of t_V as

$$t_{rh} = \frac{2\sqrt{2}\pi N}{3 \cdot 15.4 \ln(\gamma N)} t_V. \quad (4)$$

For ($N = 5000, \gamma = 0.11$) we have $t_{rh} \simeq 152 t_V$. The crossing time at the virial radius is given by $t_{cr} = 2r_V/v_m = 2\sqrt{2} t_V$.

For the data evaluation, we employed boxcar smoothing to reduce noise from our plots. We usually employed smoothing widths of $5 - 20 t_V$.

3 ISOLATED EQUAL-MASS MODELS

In this section, we study the effect of rotation on the core collapse in isolated N -body models (i.e. without tidal field) and find, that these models suggest the occurrence of the gravogyro instability, which has been found earlier in FP models. Table 1 shows our initial isolated equal-mass models.

3.1 Core collapse

For the theory of the gravothermal instability, which leads to the core collapse of star clusters we refer to the original works of Antonov (1962), Lynden-Bell & Wood (1968) and Hachisu et al. (1978a/b). It is nowadays also described in many textbooks such as Binney & Tremaine (1987) or Heggie & Hut (2003).

Figure 1 shows the time evolution of the core radius for the models of series EM2. In this series, one very fast rotating model with $\omega_0 = 0.9$ is included. The core radius is defined as

$$r_c = \sqrt{\frac{\sum_{i=1}^N |\vec{r}_i - \vec{r}_d|^2 \rho_i^2}{\sum_{i=1}^N \rho_i^2}}, \quad (5)$$

where \vec{r}_i is the position of the i th star, \vec{r}_d are the coordinates of the density center of the star cluster and ρ_i is the local density at the position of the i th star. The latter two quantities are calculated according to the description in Casertano & Hut (1985) using the distance to the fifth nearest neighbor. It can be seen in Figure 1 that the core radius decreases by two orders of magnitude and that the core collapse occurs earlier for the faster rotating models. Note that the four models of series EM2 do not exactly have the same

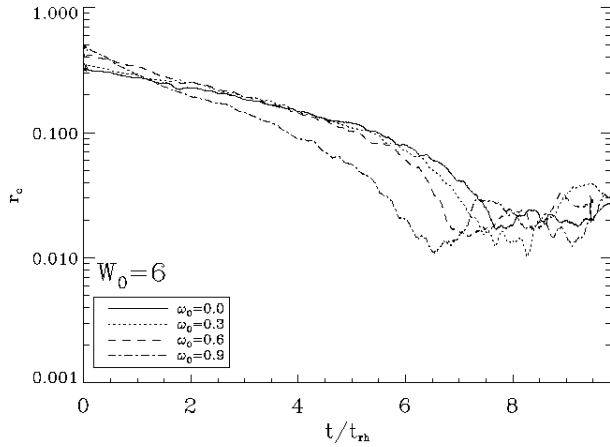


Figure 1. Time evolution of the core radius for the isolated models EM2a-d.

Gravothermal instability	Gravogyro instability
$\partial_r \sigma^2 \neq 0$	$\partial_r \omega \neq 0$
Negative specific heat capacity	Negative specific moment of inertia
Energy transport	Angular momentum transport
Heat conduction	Viscosity

Table 2. A comparison between gravothermal and gravogyro instability.

initial core radius in the beginning, i.e. the core radii differ by factors up to approximately two. This indicates that the models are indeed not in all respects exactly comparable, cf. Figures 14/15 of K02. They have slightly different density distributions corresponding to their degree of flattening. However, since the core shrinks by two orders of magnitude during the core collapse, a factor of two in the difference of the initial core radii seems to be negligible.

Figure 2 shows the time evolution of the Lagrangian radii for the models of series EM2. The inner Lagrangian radii shrink and the outer ones expand.

The last column of Table 1 contains the core collapse times for the isolated equal-mass models. The core collapse time is defined as the time when the core radius r_c reached its first sharp minimum. For the averaged runs the given time is the arithmetic mean of the core collapse times which we determined for each single run. We also give the standard deviations σ_{n-1} as a measure of the run-to-run variation of the core collapse times.

3.2 Gravogyro instability revisited - I

There is obviously a need to explain the accelerated core collapse of the rotating models in Section 3.1. A theoretical model, which explains such an effect, has been proposed as early as in the 1970s by Inagaki & Hachisu (1978) and Hachisu (1979, 1982). They called it the gravogyro instability. This instability is expected in self-gravitating and rotating systems and has been derived for self-gravitating cylinders of infinite length in z -direction: If we equate the

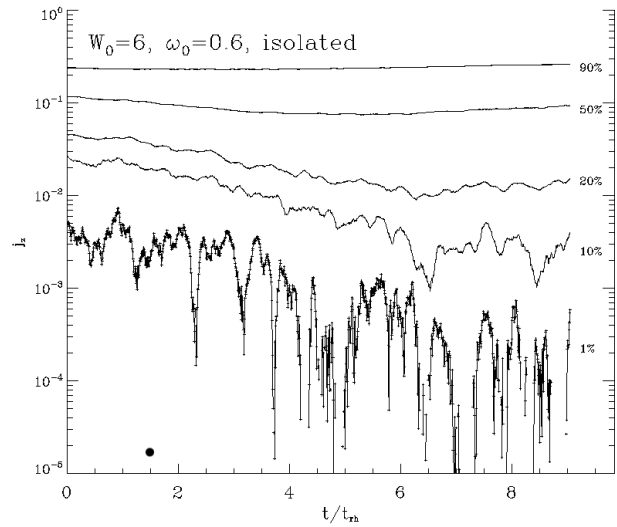


Figure 3. Time evolution of the z -component of the specific angular momentum of the particles within the Lagrangian radii for the fast rotating isolated model EM2c. The isolated points are artefacts and stem (like the interruptions in the 1% curve) from the sign change of j_z .

centrifugal force to the gravity in the equatorial plane ($z = 0, R^2 = x^2 + y^2$) and neglect the pressure gradient, we have

$$\frac{2GM_R}{R} \simeq \frac{j_z^2}{R^3}, \quad (6)$$

where M_R is the mass per unit length in z -direction contained within the radius R in cylindrical coordinates and j_z is the z -component of specific angular momentum. We readily obtain $\delta j_z / j_z \simeq \delta R / R$. Using the equation $j_z = R^2 \omega$ in addition, we obtain $\delta j_z \simeq \omega R \delta R$ and $\delta j_z = 2\omega R \delta R + R^2 \delta \omega$. The combination of these relations yields the following linear differential relation between specific angular momentum j_z and angular speed ω :

$$\delta j_z \simeq -R^2 \delta \omega. \quad (7)$$

A negative specific moment of inertia occurs in this relation, cf. Inagaki & Hachisu (1978).

If we let an initial model evolve, which exhibits a radial gradient of the angular speed and has reasonable rotation curve, angular momentum is transported outwards on the relaxation time scale by the stellar dynamical analog of viscosity. The core of the star cluster contracts because of a deficit in the centrifugal force. The angular speed in the core increases according to relation (7). A runaway departure from the initial state takes place. This cycle is what they denoted as the gravogyro instability. For a comparison between gravothermal and gravogyro instabilities see Table 2.

One may wonder: Does the gravogyro catastrophe really occur in isolated N -body models? Figure 3 shows the time evolution of the z -component of specific angular momentum within the Lagrangian radii for the fast rotating isolated model EM2c. The z -component of specific angular momentum of each star is calculated according to

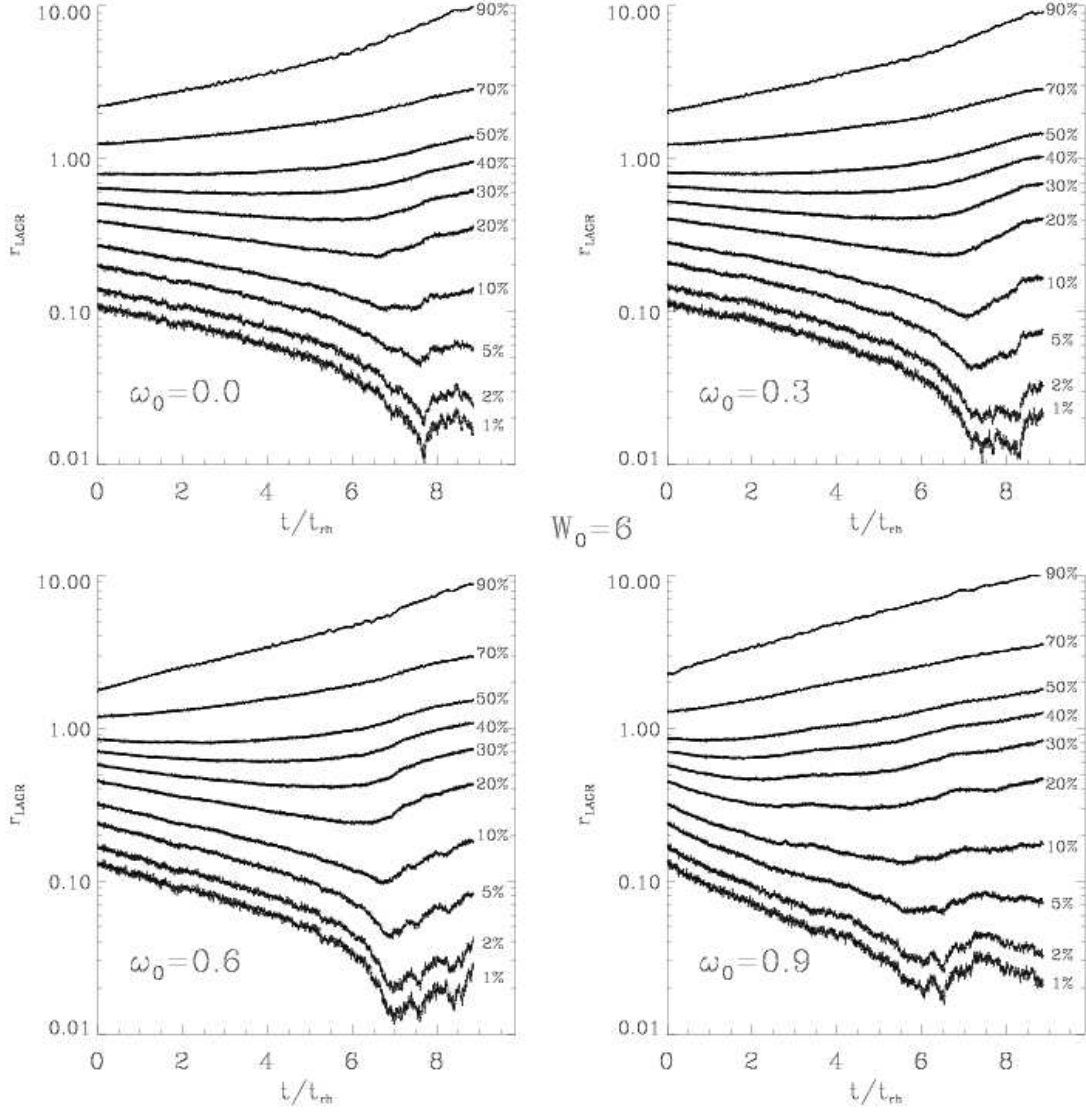


Figure 2. Time evolution of the Lagrangian radii, which contain 1%, 2%, 5%, 10%, 20%, 30%, 40%, 50%, 70% and 90% of the initial total mass of the star cluster for the isolated equal-mass models EM2a-d. The inner Lagrangian radii contract, while the outer ones expand in the core collapse phase.

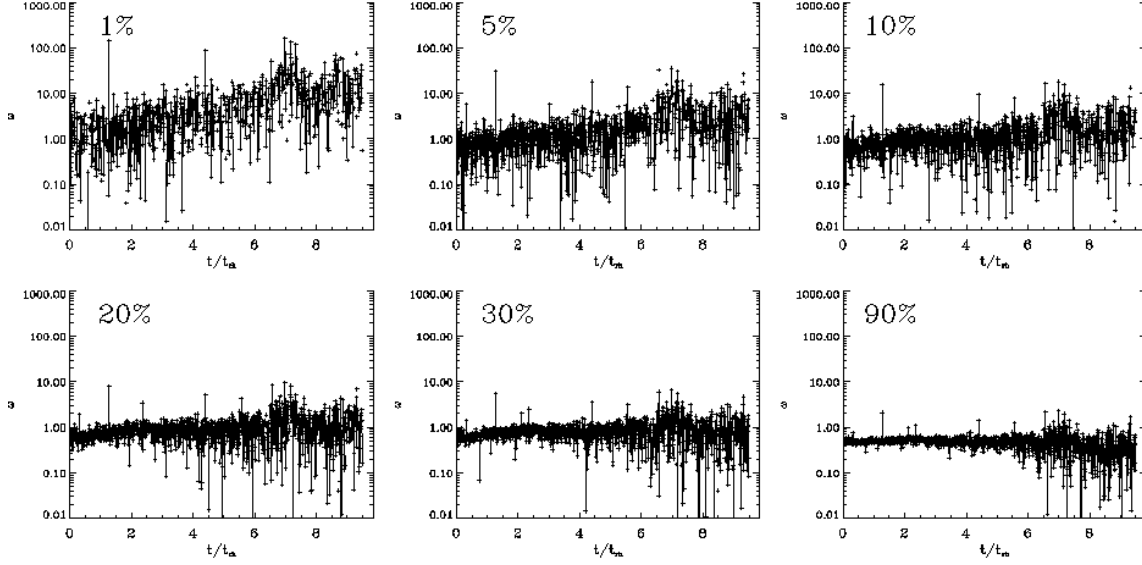


Figure 4. Time evolution of the average angular speed of the particles within the Lagrangian radii for the fast rotating isolated model EM2c with $W_0 = 6, \omega_0 = 0.6$. The interruptions and isolated points are artefacts stemming from the sign change of ω .

$$j_z = [(\vec{r}_* - \vec{r}_d) \times \vec{v}_*]_z, \quad (8)$$

where $\vec{r}_* = (x_*, y_*, z_*)$ is the position of a particle, $\vec{v}_* = (v_{*x}, v_{*y}, v_{*z})$ is its velocity and $\vec{r}_d = (x_d, y_d, z_d)$ is the density center of the star cluster. It is then summed over all particles within a given Lagrangian radius and divided by the number of particles inside that radius. One notes that angular momentum does indeed diffuse from the inner parts of the cluster to the outer parts, as time proceeds.

Now we study the evolution of the angular speed ω . The gravogyro instability implies that j_z goes down while ω increases. Figure 4 shows the time evolution of the average angular speed of the particles within the Lagrangian radii. The angular speed of one particle is calculated according to

$$\omega = \frac{j_z}{R_*^2} = \frac{[(\vec{r}_* - \vec{r}_d) \times \vec{v}_*]_z}{R_*^2}, \quad (9)$$

with the same notations as in equation (8), but $R_* = \sqrt{(x_* - x_d)^2 + (y_* - y_d)^2}$ is the radius with respect to the density center in cylindrical coordinates. It is then summed over all particles inside a given Lagrangian radius and divided by the number of particles within that radius. One can observe an increasing average angular speed inside those Lagrangian radii, which show a decrease in the z -component of angular momentum. Thus, it is shown that gravogyro effects appear in our isolated models.

4 TIDALLY LIMITED EQUAL-MASS MODELS

As a step towards more realistic models of globular clusters, we investigate in this section the effects of the tidal field of the Galaxy on the dynamical evolution of rotating globular clusters. The implementation of the tidal field of the Milky Way Galaxy within the tidal approximation used in NBODY6 and NBODY6++ is in detail described in Appendix A. Different escape criteria are discussed in Appendix B. In our

Model	W_0	ω_0	N	Averaging	t_{cc}/t_{rh}
EM3a	6	0.0	5K	4	7.11 ± 0.37
EM3b	6	0.3	5K	4	6.37 ± 0.36
EM3c	6	0.6	5K	4	5.42 ± 0.33
EM3d	6	0.9	5K	4	3.97 ± 0.40
EM4b	6	-0.3	5K	4	6.50 ± 0.33
EM4c	6	-0.6	5K	4	5.62 ± 0.07
EM4d	6	-0.9	5K	4	4.88 ± 0.28

Table 3. The initial tidally limited equal-mass models. The rotating models of series EM3 are prograde rotating while the models of series EM4 are retrograde rotating with respect to the orbit of the star cluster around the Galaxy. We also give the run-to-run variation σ_{n-1} in t_{cc}/t_{rh} in the last column.

models, the star cluster initially completely fills its Roche lobe in the tidal field of the Galaxy. In other words, the density of the initial rotating King model approaches zero at the physical tidal cutoff radius. The tidal radius is defined as the distance of the star cluster center to the Lagrangian points L_1/L_2 .

Table 3 shows the initial tidally limited equal-mass models. The model of series EM3 are prograde rotating, i.e. the stars move around the z -axis of the cluster-centered coordinate system in the same sense as the star cluster moves around the Galaxy. The models of series EM5 are retrograde rotating, which we denoted by a negative sign of the rotation parameter ω_0 for clarity. The only difference between the rotating initial models of series EM3 and EM4 is that we reversed the sign of all initial velocity vectors.

4.1 Core collapse

Figure 6 shows the time evolution of the core radius for the prograde rotating tidally limited models EM3a-d. A comparison of Figures 1 and 6 and the core collapse times in Tables 1 and 3 shows, that the tidal field further accelerates

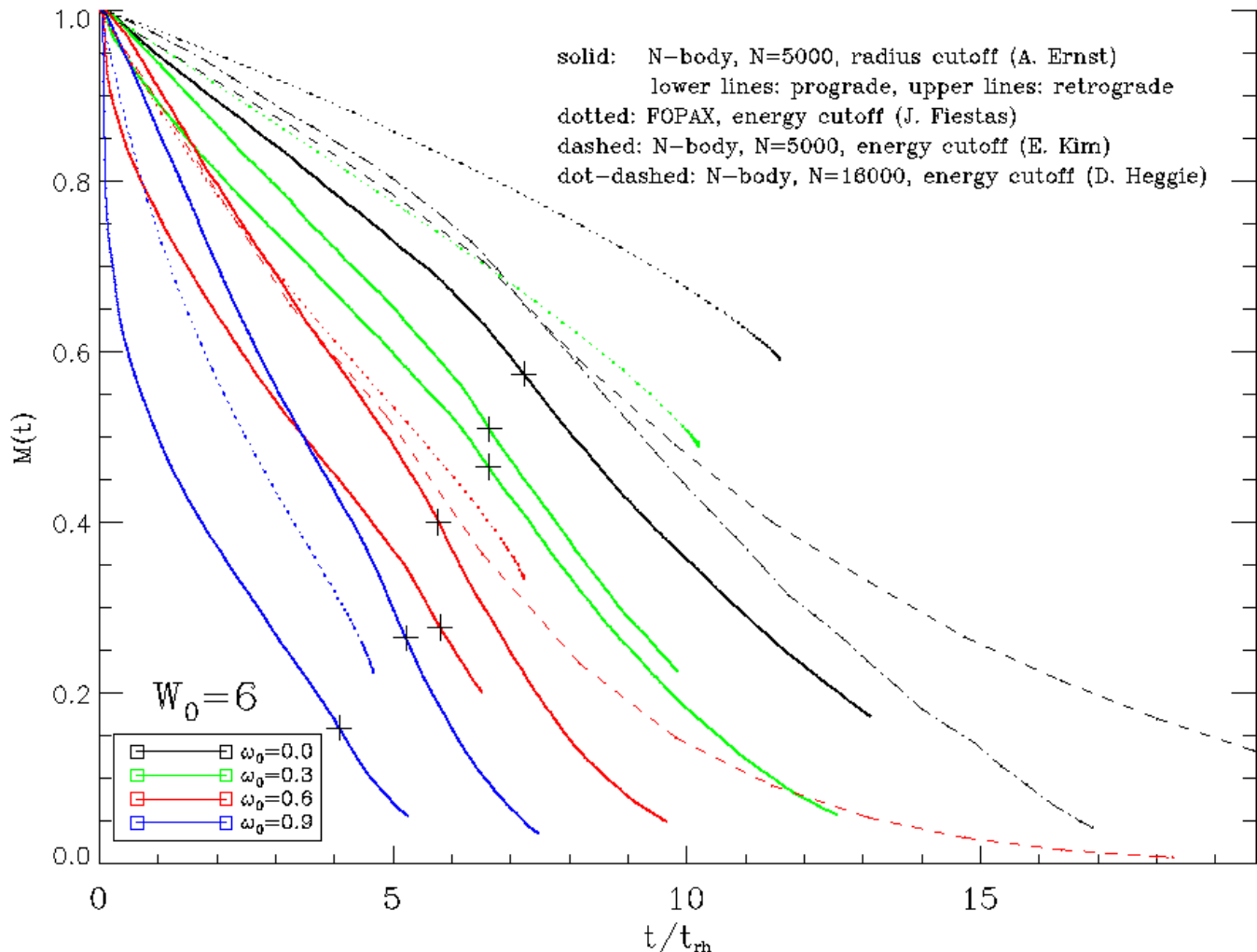


Figure 5. Time evolution of the total mass of the star clusters for the prograde rotating tidally limited models EM3a-d (lower solid lines), the retrograde rotating tidally limited models EM4b-c (upper solid lines), FP models with energy cutoff (dotted), two N -body models with $N = 5000$ and energy cutoff (dashed) and one non-rotating N -body model with $N = 16000$ and energy cutoff (dot-dashed). The core collapse times of our N -body models are marked with a cross.

the core collapse by a significant amount. The reason for this behaviour is that rapid mass loss across the tidal boundary provides an additional mechanism for the transport and removal of energy and angular momentum, thus enhancing the effects of the gravothermal and gravogyro instabilities. An inspection of Table 3 reveals that there is a difference between the core collapse times between the models of series EM3 and EM4, i.e. the prograde rotating models of series EM3 collapse faster than the retrograde rotating model of series EM4. By considering the run-to-run variation σ_{n-1} in the last column of table 3, we see that the statistical significance of this effect is strongest for the two models with $\omega_0 = 0.9$ as compared with the case of the slower rotating models. Therefore this effect might be related to the formation of a bar in the fastest rotating models. On the other hand, the difference of the core collapse times between the prograde and retrograde rotating models may also be related to the difference in the rates of mass loss (see next Section): The loss of energy and angular momentum through escaping stars is more rapid for the prograde rotating models and thus

the effects of the gravothermal and gravogyro instabilities, which accelerate the core collapse, are stronger.

4.2 Mass loss

Figure 5 shows the time evolution of the total mass of the globular clusters, where the initial mass is normalized to one, for several models, including simulations with the 2D FP code FOPAX (with energy cutoff, cf. Fiestas 2006), one rotating and one non-rotating N -body model by E. Kim (with energy cutoff, without the tidal approximation, see K03) and one non-rotating N -body model by D. C. Heggie (with energy cutoff, without the tidal approximation). The solid lines are our NBODY6++ results (with radius cutoff and the tidal approximation). The different “cutoffs” are explained in Appendix B. The initial models are the same rotating (or non-rotating) King models. Note that for the rotating models, there are two solid lines for each color. The lower of these lines corresponds to a prograde rotating model (i.e., from series EM3). The upper of these lines corresponds to a retrograde rotating model (i.e., from series EM4). The

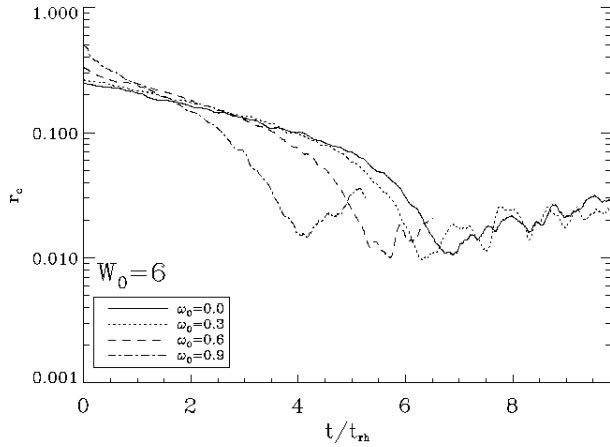


Figure 6. Time evolution of the core radius for the prograde rotating tidally limited models EM3a-d

escape rate for retrograde rotating models is considerably lower, since many stars in retrograde orbits are subject to a “third integral” of motion, which restricts their accessible phase space and hinders them from escaping, see Fukushima & Heggie (2000) and Appendix B.

Figure 5 also shows, that the faster rotating models suffer stronger mass loss than the slowly or non-rotating models, a fact which has already been shown in the FP models of ES99.

The differences between the models of the same rotation parameter are due to different implementations of the tidal field in the various codes (cf. Appendix B) or due to the different modelling techniques in general. For instance, the difference between the N -body and FP models is the tidal approximation used in NBODY6 and NBODY6++, i.e. the modified equations of motion with a linear approximation of the tidal forces (see Appendix A), a feature, which cannot be implemented in an FP code, which relies only on a tidal cutoff. The geometry of the almond-shaped tidal boundary within the tidal approximation (see Figure B1) differs from the geometry of our star cluster models, which are axisymmetric. This may cause another difference between N -body and FP models. In addition, the difference between prograde and retrograde rotating models cannot be seen in FP models. Note that Kim et al. (2006) use for their comparison N -body models with an artificially implemented tidal cutoff and no modification of the equations of motion.

Last but not least, a further inspection of Figure 5 reveals, that core collapse causes an increase in the escape rate, i.e. short before the core collapse time the curves steepen slightly. The moment of core collapse is marked with a cross on each curve corresponding to one of our N -body models. However, our main aim was to show the difference of prograde and retrograde rotating models and the fact, that rotation significantly increases the rate of mass loss.

4.3 Gravogyro instability revisited - II

In this subsection, we briefly look at the gravogyro instability in the tidally limited N -body models. The mass loss through the tidal boundary provides, as noted before, an additional mechanism for the transport and removal of an-

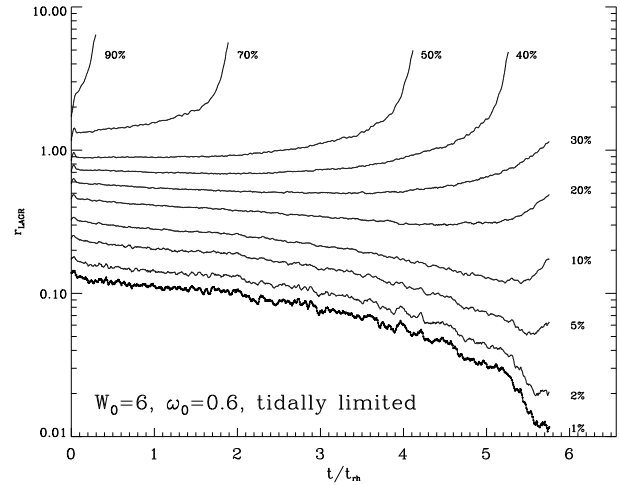


Figure 7. Time evolution of the Lagrangian radii for a single run of the fast rotating tidally limited model EM3c. For explanations see the text.

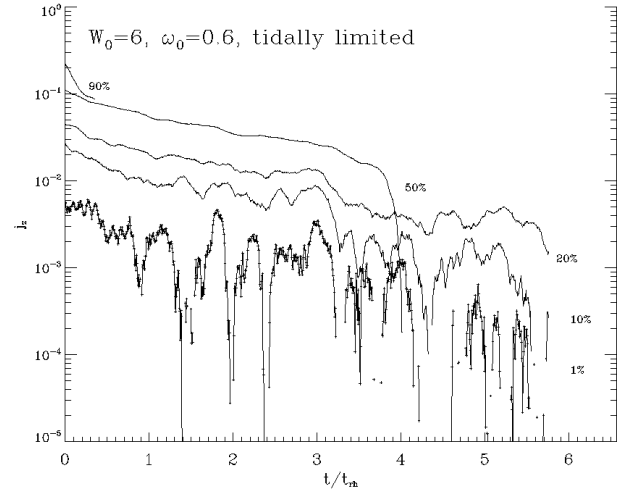


Figure 8. Time evolution of the z -component of the specific angular momentum of the particles within the Lagrangian radii for a single run of the fast rotating tidally limited model EM3c. For explanations see the text.

gular momentum (besides viscosity effects). Figure 7 shows the time evolution of the Lagrangian radii for one run of the tidally limited model EM3c. The Lagrangian radii are defined with respect to the initial particle number. Therefore the particle number within the Lagrangian radii remains constant while the system evolves, whereas after some time, the outer Lagrangian shells are completely lost due to escaping stars, i.e. the curves for the outer Lagrangian radii bend upwards until they reach twice the tidal radius, which is the cutoff radius in the adopted escape criterion. Figure 8 shows the time evolution of the z -component of specific angular momentum within the Lagrangian radii for the same single run of the tidally limited model EM3c. The curves for j_z decrease due to escaping stars carrying away angular momentum. The curves stop at the point at which the adjacent outer Lagrangian shell is lost, such that we always have a constant particle number within the Lagrangian radii. Figure 9 shows the time evolution of the average angular speed

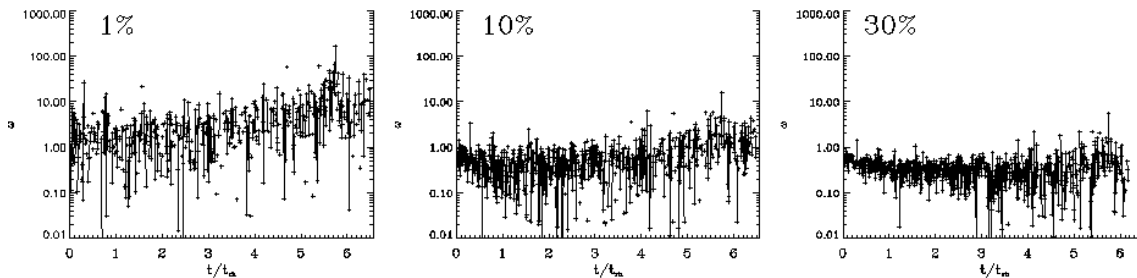


Figure 9. Time evolution of the average angular speed of the particles within the Lagrangian radii for a single run of the fast rotating tidally limited model EM3c with $W_0 = 6$, $\omega_0 = 0.6$. For explanations see the text.

of the stars within the Lagrangian radii for the same single run of the tidally limited model EM3c. After an initial decrease of ω due to mass loss, which is most prominent in the outer Lagrangian spheres but reaches deep into the core, ω increases more than in the isolated model and up to higher radii. A similar effect can be seen in FP models, see Einsel (1996), Figures 40 and 42.

5 ISOLATED TWO-MASS MODELS

Realistic globular clusters have a mass spectrum. However, the main effects of a mass spectrum on the dynamics of globular clusters can already be seen in idealized models composed out of only two mass components. We study such models in this section. Table 4 summarizes our initial models with two mass components. All these models are done with NBODY6++. We would like to stress that they are isolated, and no averaging was used. The total mass fraction of heavy stars q was fixed to the value $q = 0.1$ as for the largest part of the parameter space covered in Khalisi (2002) and Khalisi et al. (2006). As he notes, this choice was inspired by a result of Inagaki & Wiyanto (1984) that a cluster evolves fastest for $q = 0.1$. Following the work of Khalisi, we varied the stellar mass ratio μ . The models of series TM9 and TM10 with high particle numbers ($N=32K$) were computed (using 32-128 processors) at the IBM Regatta p690+ supercomputer “Jump” at the Research Center Jülich, consisting of a total of 1312 Power4+ processors running at a frequency of 1.7 GHz, whereas the models of series TM11 and TM12 (also $N=32K$) were computed with the PC Beowulf cluster “Hydra” of the ARI, consisting of 10 Dual P4 with 2.2 GHz. Each of the core collapse times given in Table 4 is the arithmetic mean of three times which were determined for each run: When the core radius had its first sharp minimum, the minimum potential in the star cluster reached its first sharp minimum and the maximum density in the core reached its first sharp maximum.

Figure 10 shows the time evolution of the Lagrangian radii for the model TM7a, computed separately for the light/heavy component. While the orbits of the light stars expand, the heavy stars sink to the center. As can be seen, only the heavy masses are involved in the core collapse. For the non-rotating case with $q = 0.1$, the transition between the Spitzer-stable and Spitzer-unstable regimes lies indeed between $\mu = 1.25$ and $\mu = 2$, as we checked in our data. For details on the Spitzer instability, see the original work of Spitzer (1969) or the review in Khalisi (2002). The em-

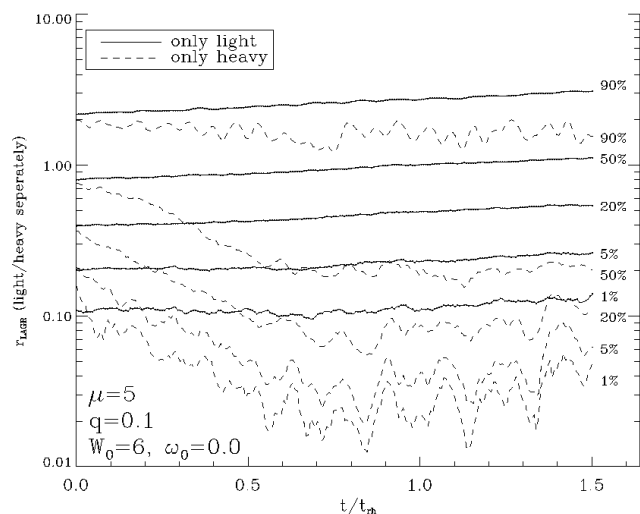


Figure 10. Time evolution of the Lagrangian radii of the model TM7a, computed separately for the light masses, neglecting the heavy masses and for the heavy masses, neglecting the light masses. In particular, this Figure shows the radii, in which 1%, ..., 90% of the light/heavy masses are contained.

pirical criterion by Watters et al. (2000), which is based on Monte-Carlo simulations, also yields a transition occurring between the above values of μ .

Figure 11 shows the evolution of the maximal density in the core for the models of series TM5 – TM8 and TM11 – TM12. What can immediately be seen in Figure 11 is the acceleration of the core collapse due to mass segregation. The higher the stellar mass ratio μ , the shorter is the core collapse time.

Figure 12 shows the acceleration factor of the core collapse due to mass segregation. For this plot we used the equal-mass core collapse times $t_{cc,1}$ of the non-rotating isolated models EM1a and EM2a (see Section 3) and the core collapse times $t_{cc,\mu}$ from the non-rotating models “a” of series TM1-TM12. Khalisi and Spurzem (2001) confirmed the relation

$$t_{cc,\mu} \propto t_{cc,1}/\mu, \quad (10)$$

which is derived from the relevant time scales and also shown in Figure 12. In the limit of small μ the curve approaches the Spitzer-stable regime while in the limit of large μ N -dependant effects play a role, which can be seen in more detail in the study by Khalisi et al. (2006) (their Figure 6).

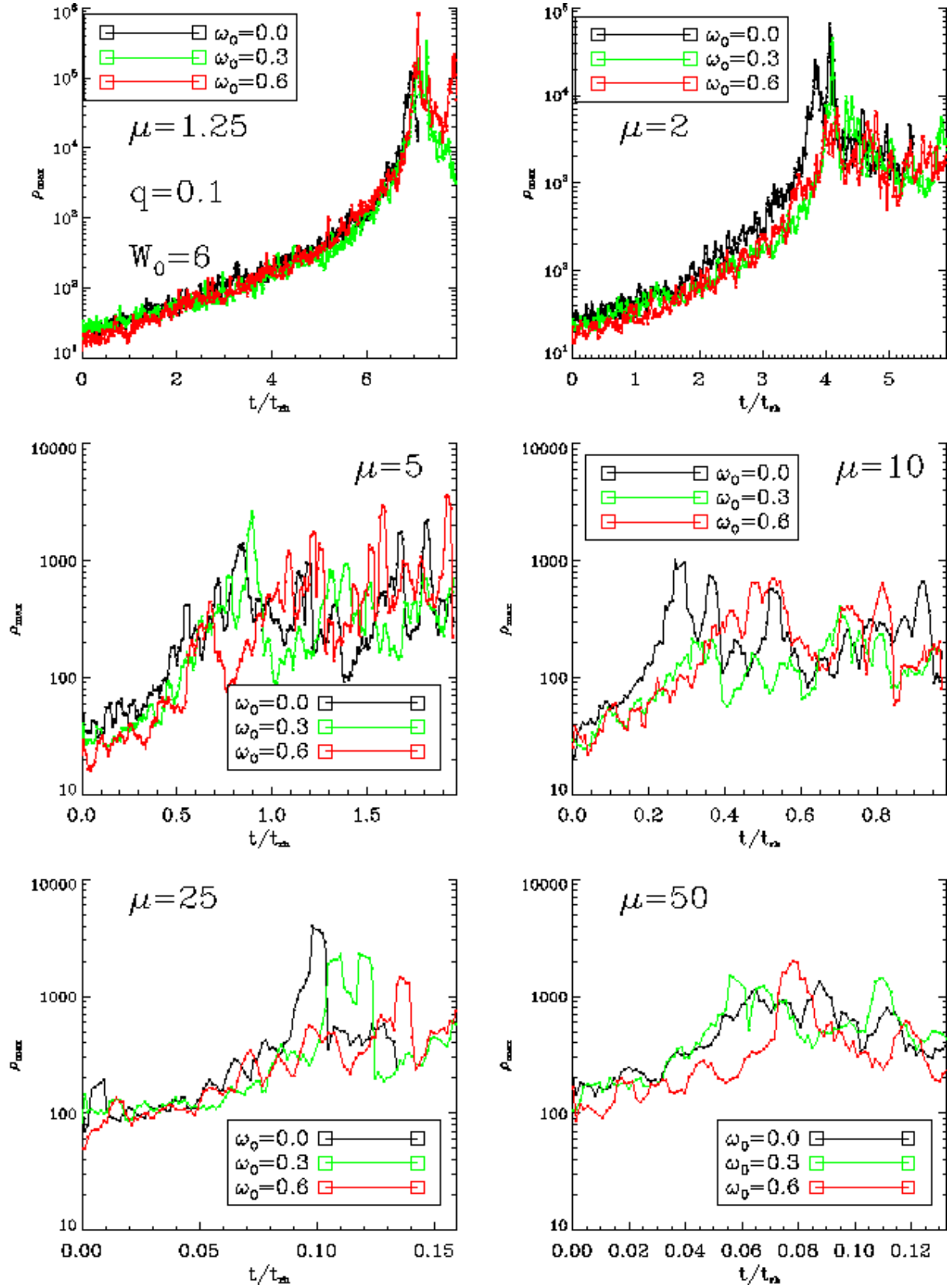


Figure 11. Time evolution of the maximal density in the core for the models of series TM5 – TM8 and TM11 – TM12

Model	W_0	ω_0	N	μ	q	t_{cc}/t_{rh}	Model	W_0	ω_0	N	μ	q	t_{cc}/t_{rh}
TM1a	3	0.0	5K	1.25	0.1	9.07	TM2a	3	0.0	5K	2	0.1	5.38
TM1b	3	0.3	5K	1.25	0.1	9.77	TM2b	3	0.3	5K	2	0.1	5.49
TM1c	3	0.6	5K	1.25	0.1	9.92	TM2c	3	0.6	5K	2	0.1	5.93
TM3a	3	0.0	5K	5	0.1	1.30	TM4a	3	0.0	5K	10	0.1	0.93
TM3b	3	0.3	5K	5	0.1	1.43	TM4b	3	0.3	5K	10	0.1	0.71
TM3c	3	0.6	5K	5	0.1	1.39	TM4c	3	0.6	5K	10	0.1	0.80
TM5a	6	0.0	5K	1.25	0.1	6.94	TM6a	6	0.0	5K	2	0.1	3.86
TM5b	6	0.3	5K	1.25	0.1	7.25	TM6b	6	0.3	5K	2	0.1	4.09
TM5c	6	0.6	5K	1.25	0.1	7.08	TM6c	6	0.6	5K	2	0.1	4.16
TM7a	6	0.0	5K	5	0.1	0.84	TM8a	6	0.0	5K	10	0.1	0.28
TM7b	6	0.3	5K	5	0.1	0.89	TM8b	6	0.3	5K	10	0.1	0.31
TM7c	6	0.6	5K	5	0.1	1.21	TM8c	6	0.6	5K	10	0.1	0.51
TM9a	3	0.0	32K	25	0.1	0.27	TM10a	3	0.0	32K	50	0.1	0.26
TM9b	3	0.3	32K	25	0.1	0.37	TM10b	3	0.3	32K	50	0.1	0.22
TM9c	3	0.6	32K	25	0.1	0.31	TM10c	3	0.6	32K	50	0.1	-
TM11a	6	0.0	32K	25	0.1	0.10	TM12a	6	0.0	32K	50	0.1	0.06
TM11b	6	0.3	32K	25	0.1	0.12	TM12b	6	0.3	32K	50	0.1	0.07
TM11c	6	0.6	32K	25	0.1	0.13	TM12c	6	0.6	32K	50	0.1	0.08

Table 4. The initial models with two mass components.

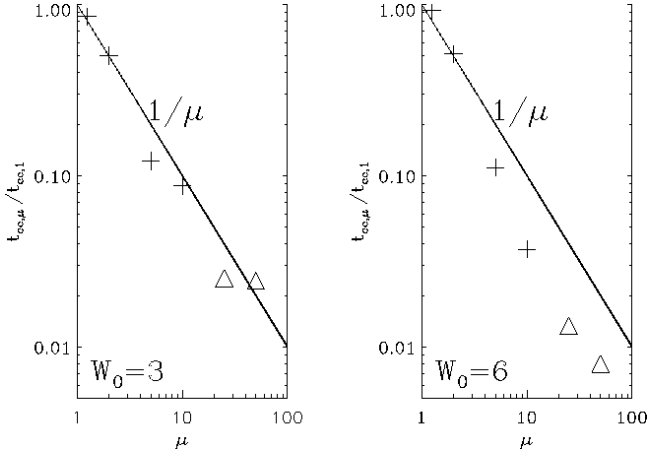


Figure 12. Acceleration factor of the core collapse due to mass segregation. The positions of the crosses ($N=5000$) and triangles ($N=32000$) are calculated from values in Table 4 for the non-rotating models and normalized to values in Table 1 for the equal-mass models ($\mu = 1$).

However, in Figure 11 the acceleration of the core collapse due to rotation is not detectable. Rather, by also taking into account the core collapse times in columns 7 and 14 of Table 4, it seems, that in most models, there is an opposite effect, i.e. the rotating models have a delayed core collapse.

Figure 13 shows the time evolution of the Lagrangian radii for the models TM7a and TM7c, computed only for the heavy masses. A comparison of the curves for the models with different ω_0 in Figure 13 reveals that the inner ($\lesssim 50\%$) Lagrangian radii for the model ($\omega_0 = 0.6$) decrease somewhat slower than those of the non-rotating model ($\omega_0 = 0.0$). This points towards a slowdown of the mass segregation process induced by rotation.

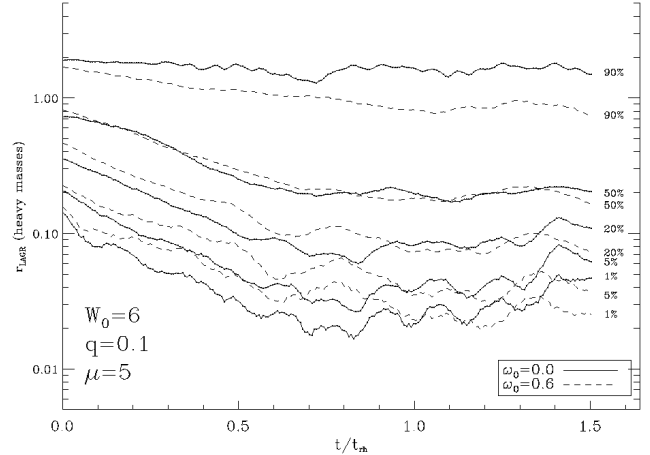


Figure 13. Time evolution of the Lagrangian radii of the models TM7a and TM7c, computed only for the heavy masses, neglecting the light masses.

Figure 14 illustrates the time evolution of the z -component of angular momentum contained within the core, the half-mass radius and the 90% Lagrangian radius for the two mass species separately for the isolated model TM6c. For each color, the upper curve corresponds to the light masses, while the lower curve corresponds to the heavy masses. Note that the z -component of the total angular momentum remains approximately constant, since the model is isolated. The core loses angular momentum to the outer parts of the cluster. Kim et al. point out, that angular momentum is transferred from the high masses to the low masses. We cannot prove this trend in Figure 14. As we consider the angular momentum contained in the core, it can be seen that the high masses and the low masses as well lose angular momentum. The angular momentum loss of the heavy

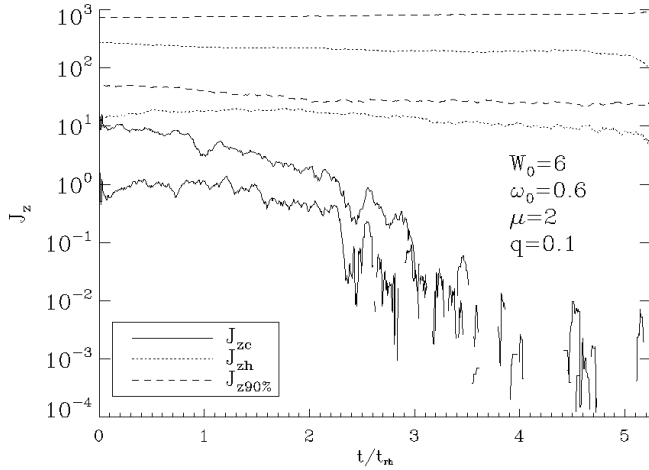


Figure 14. Time evolution of the z -component of angular momentum contained within the core, the half-mass radius and the 90% Lagrangian radius, separately for the two mass components (for each linestyle: upper curve: light, lower curve: heavy) for the model TM6c. The interruptions in the black curves stem from the sign change of the plotted quantity.

masses is a bit slower than that of the light masses which is still in accordance with K04 (see their Figure 11).

At last, we would like to mention that we checked the pairing of the dynamically formed binaries in our two-mass models. In the Spitzer-stable regime ($\mu = 1.25$) all pairings occur: Heavy-heavy, light-light and heavy-light. The pairings change from time to time. In the Spitzer-unstable regime of our parameter space ($\mu = 2-50$), we noticed (with a few exceptions) only heavy-heavy binaries.

6 DISCUSSION

The main aim of this paper was to investigate the effect of an overall (differential) rotation on the dynamical evolution of globular clusters with direct N -body models. We would like to briefly summarize our results first and then tackle a comparison with results obtained by others.

6.1 Summary

The difference between rotating and non-rotating equal-mass N -body models of globular clusters is that an overall (differential) rotation accelerates their dynamical evolution. For instance, the core collapse of equal-mass models is accelerated for the cases with rotation as compared with the non-rotating models. However, this acceleration of the dynamical evolution induced by rotation cannot be seen in our isolated two-mass N -body models.

As can be seen in Table 1, the core collapse times are larger for the models with King parameter $W_0 = 3$ than for those with $W_0 = 6$, which are more concentrated. This is a well-known fact, which is noted, for instance, in Quinlan (1996) or Gürkan et al. (2004). For the models EM1a-c with $W_0 = 3$, the acceleration of the core collapse due to rotation is not visible within the estimated error margins of the measurement. Therefore, runs with higher particle numbers are required, or, an averaging over several runs with different

initial configurations of positions and velocities, which has been done for the models EM2a-d with $W_0 = 6$ in order to damp statistical fluctuations.

In the tidally limited models, we observe rapid mass loss across the tidal boundary, which is stronger for the faster rotating models. A tidal field further accelerates the core collapse, since it provides an additional mechanism for the transport and removal of energy and angular momentum through escaping stars, thus enhancing the effects of the gravothermal and gravogyro instabilities.

In the case of tidally limited N -body models within the tidal approximation (see Appendix A), the sense of rotation plays an important role in the escape process. Models, where most stars are in retrograde orbits (as compared with the sense of rotation of the star cluster around the galaxy), have a significantly lower escape rate due to the presence of a “third integral”, cf. Fukushige & Heggie (2000) and Appendix B.

The gravogyro instability predicted by Inagaki & Hachisu (1978) and Hachisu (1979, 1982), as it becomes manifest in a decrease of the z -component of angular momentum combined with an increase in the angular speed, was found in both isolated and tidally limited equal-mass N -body models.

In the models with two mass components, mass segregation takes place, which again accelerates the dynamical evolution of the globular cluster and results in a faster core collapse, the higher the stellar mass ratio μ is. Our results are in fair agreement with results in Khalisi et al. (2006).

However, if both mass segregation and rotation compete in the acceleration of the dynamical evolution of the globular cluster, the trend that rotation accelerates the dynamical evolution of the stellar system, is no more visible in isolated models. Rather, in most models, there seems to be an opposite effect: The faster rotating isolated models have a delayed core collapse as compared with the non-rotating models. A possible explanation is that the rotation slows down the mass segregation process. However, the statistical quality of our results is limited.

6.2 Comparisons with other N -body models

A few N -body models of rotating globular clusters have been presented in chapter 4 of K03. This chapter is a comparative study between N -body simulations and FP model results; see also the recent work by Kim et al. (2006) [hereafter: K06]. Kim’s initial models are the same rotating King models as they are described in Section 2. He used a version of Aarseth’s original code NBODY6 modified “to mimic the tidal environment of the clusters modeled with the 2D FP equation.” Namely, he applied a tidal energy cutoff to his N -body models (see Appendix B). With the same definition of relaxation time, the half-mass times of his and our N -body models differ significantly, as can be seen in Figure 5. The same is valid for a comparison of the half-mass times of our non-rotating N -body model and the corresponding N -body model by Heggie (also with energy cutoff). The reason for these rather large differences is the different treatment of the tidal field. The core collapse times from our N -body models agree well with those of Kim’s N -body models. Our results are also consistent with N -body simulations presented in

Ardi et al. (2005, 2006) if the same definition of the half-mass relaxation time is used.

6.3 Comparison with FP models

For a comparative study of N -body models of rotating star clusters with FP models we refer to chapter 4 of K03 and the recent work K06. While the time step in N -body simulations is a fraction of the orbital time, it is a fraction of relaxation time in the FP codes used in ES99 and K02, K03, K04 and K06. Therefore, the proper definition of relaxation time is crucial for a comparison of N -body and FP models. With equation (4) as definition of the half-mass relaxation time, the core collapse times in our equal-mass N -body models (i.e. the models of series EM1–EM4) are shorter than the core collapse times in the tidally limited FP models in ES99 (see their Figure 2) and the isolated FP models in K02 (see their Figure 3). A similar trend has been found in K03 and K06.

The different implementations of a tidal boundary in N -body and FP models and the absence of tidal forces in FP models have a significant influence on the escape rates (see Section 4.2 and Figure 5).

In the models with two mass components, a difference to FP models of K04 occurs: In our isolated models, we do not see the effect of acceleration of the core collapse due to rotation any more.

6.4 Future work

Several questions remained unanswered – the endeavor to answer some of the following questions may be the starting point for future investigations: Does the suspected slow-down of the mass segregation process induced by rotation also occur in tidally limited models with two mass components? How evolves the average angular speed of the different mass components, taken separately? We need a more intensive N -body study of tidally limited rotating systems with a mass spectrum and a better statistical quality, i.e. higher particle numbers or extensive averaging. How do stellar evolution, disk shocking, primordial binaries or a central black hole influence the dynamical evolution of rotating globular clusters?

ACKNOWLEDGMENTS

We are indebted to Sverre Aarseth for the provision of NBODY6. Furthermore, the authors would like to thank Eunhyeuk Kim and Douglas Heggie for providing some of their N -body models with energy cutoff for comparison, Peter Berczik for his help with the determination of the critical ω_0 for which isolated rotating King models become unstable to the formation of a bar and Marc Freitag for his helpful comments. AE was supported by the International Max Planck Research School for Astronomy and Cosmic Physics (IMPRS) at the University of Heidelberg and would like to thank Jonathan M. B. Downing for a discussion. We acknowledge computing time at the supercomputer “Jump” at the NIC Jülich, Germany. The PC cluster “Hydra” at the ARI (funded by the SFB 439, University of Heidelberg) was also used.

REFERENCES

- Aarseth S. J., MNRAS 144, 537 (1969)
- Aarseth S. J., Publ. Astron. Soc. Pacific 111, 1333 (1999)
- Aarseth S. J., *Gravitational N-body simulations – Tools and Algorithms*, Cambridge Univ. Press (2003)
- Aguirre J., Vallejo J. C., Sanjuán M. A. F., Phys. Rev. E 64, 066208 (2001)
- Aguirre J., Sanjuán M. A. F., Phys. Rev. E 67, 056201 (2003)
- Ahmad A., Cohen L., J. Comp. Phys. 12, 389 (1973)
- Akiyama K., Sugimoto D., PASJ 41, 991 (1989)
- Allen C., Moreno E., Pichardo B., Ap. J. 652, 1150 (2006)
- Anderson J., King, I. R., AJ 126, 772 (2003)
- Antonov V. A. Scient. Trans. Leningrad Univ. 20, 19 (1962)
- Ardi E., Spurzem R., Mineshige S., J. Korean Astron. Soc. 38, 207 (2005)
- Ardi E., Spurzem R., Mineshige S., submitted to PASJ (2006)
- Baumgardt H., MNRAS 325, 1323 (2001)
- Binney J., Tremaine S., *Galactic Dynamics*, Princeton Univ. Press (1987)
- Casertano S., Hut P., Ap. J. 298, 80 (1985)
- Chernoff, D. F., Weinberg, M. D., Ap. J. 351, 121 (1990)
- Dinescu D. I., Girard T. M., Altena W. F., Ap. J. 117, 1792 (1999)
- Einsel C., PhD thesis, University of Kiel (1996)
- Einsel C., Spurzem R., MNRAS 302, 81-95 (1999)
- Fiestas J., PhD thesis, University of Heidelberg (2006), <http://www.ub.uni-heidelberg.de/archiv/6145/>
- Fiestas J., Spurzem R., Kim E., MNRAS 373, 677 (2006)
- Frenk C. S. Fall S. M., MNRAS 199, 565 (1982)
- Fukushige T., Heggie D. C., MNRAS 318, 753 (2000)
- Gebhardt K., Pryor C., Williams T. B., Hesser J. E., AJ 107, 2067 (1994)
- Gebhardt K., Pryor C., Williams T. B., Hesser J. E., AJ 110, 1699 (1995)
- Gebhardt K., Pryor C., O’Connell R. D., Williams T.B., Hesser J. E., Ap. J. 119, 1268 (2000)
- Geisler D., Hodge P., Ap. J. 242, 66 (1980)
- Geyer E. H., Hopp U., Nelles B., A&A 125, 359 (1983)
- Giersz M., Heggie D. C., MNRAS 268, 257 (1994a)
- Giersz M., Heggie D. C., MNRAS 270, 298 (1994b)
- Giersz M., Heggie D. C., MNRAS 279, 1037 (1996)
- Goodman J. J., PhD thesis, Princeton University (1983)
- Gürkan A. M., Freitag M., Rasio F. A., Ap. J. 604, 632 (2004)
- Hachisu I. Sugimoto D., Prog. Theor. Phys. 60, 123 (1978a)
- Hachisu I., Nakada Y., Nomoto K., Sugimoto D., Prog. Theor. Phys. 60, 393 (1978b)
- Hachisu I., PASJ 31, 523-540 (1979)
- Hachisu I., PASJ 34, 313-335 (1982)
- Harris W. E., AJ 112, 1487 (1996)
- Heggie D. C., Mathieu R. D. in LNP 267: *The Use of Supercomputers in Stellar Dynamics Standardised Units and Time Scales*, p. 233
- Heggie D. C., Hut P., *The Gravitational Million-Body Problem*, Cambridge Univ. Press (2003), chapter 12
- Inagaki S., Hachisu, I., PASJ 30, 39-55 (1978)
- Inagaki S., Wiyanto P., PASJ 36, 391 (1984)
- Kustaanheimo P., Stiefel E. L., J. für reine angewandte Mathematik 218, 204 (1965)

Khalisi E., Spurzem R., ASP Conf. Ser. 228, 479 (2001)
 Khalisi E., PhD thesis, University of Heidelberg (2002),
<http://www.ub.uni-heidelberg.de/archiv/3096/>
 Khalisi E., Amaro-Seoane P., Spurzem R., submitted to MNRAS, astro-ph/0602570
 Kim E., Einsel C., Lee H. M., Spurzem R., Lee M. G., MNRAS 334, 310 (2002)
 Kim E., *Dynamical Evolution of Rotating Star Clusters*, PhD thesis, Seoul National University (2003)
 Kim E., Lee H. M., Spurzem R., MNRAS 351, 220 (2004)
 Kim E., Yoon I., Lee H. M., Spurzem R., in prep.
 King I. R., AJ 67, 471 (1962)
 Lagoute C., Longaretti P. Y., A&A 308, 441 (1996)
 Lee H. M., Ostriker J. P., Ap. J. 322, 123 (1987)
 Longaretti P. Y., Lagoute C., A&A 308, 453 (1996)
 Lynden-Bell D., Wood R., MNRAS 138, 495 (1968)
 MacKay R. S., Phys. Lett. A 145, 425 (1990)
 Makino J., Aarseth S. J., PASJ 44, 141 (1992)
 Mayor M. et al., A&A 134, 118 (1984)
 Meylan G., Mayor M., A&A 166, 122 (1986)
 Meylan G., Heggie D. C., Astron. Astrophys. Rev. 8, 1 (1997)
 Mikkola S., Aarseth S. J., Cel. Mech. Dyn. Astron. 47, 375 (1990)
 Mikkola S., Aarseth S. J., Cel. Mech. Dyn. Astron. 57, 439 (1993)
 Mikkola S., Aarseth S. J., Cel. Mech. Dyn. Astron. 64, 197 (1996)
 Mikkola S., Aarseth S. J., New Astronomy 3, 309 (1998)
 Oort J. H., *Stellar Dynamics*, in: *Galactic Structure*, eds. A. Blaauw & M. Schmidt, Univ. Chicago Press (1965), p. 455
 Peterson R. C., Cudworth K. M., Ap. J. 420, 612 (1994)
 Prendergast K. H., Tomer E., AJ 75, 674 (1970)
 Quinlan G. D., New Astronomy 1, 255 (1996)
 Reijns R. A. et al., A&A 445, 503 (2006)
 Shapley H., *Star Clusters*, McGraw-Hill (1930)
 Spitzer L. Jr., Ap. J. 158, L139 (1969)
 Spitzer L. Jr., Hart M. H., Ap. J. 164, 399 (1971)
 Spurzem R., J. Comp. Applied Maths. 109, 407 (1999)
 Staneva A., Spassova N., Golev V., A&A 116, 447 (1996)
 Takahashi K., Lee H. M., Inagaki S., MNRAS 292, 331 (1997)
 Takahashi K., Portegies Zwart S. F., Ap. J. 503, L49 (1998)
 van Leeuwen F. et al., A&A 360, 472 (2000)
 Watters W. A., Joshi K. J., Rasio F. A., Ap. J. 539, 331 (2000)
 White R. E., Shawl S. J., Ap. J. 317, 246 (1987)
 Wielen R., *On the lifetimes of galactic clusters*, in: *Gravitational N-body problem*, ed. M. Lecar, Proceedings of IAU Colloquium 10, Reidel Publishing Company (1972)
 Wielen R., *The Gravitational N-body Problem for Star Clusters*, in: *Stars and the Milky Way System*, Proceedings of the First European Astronomical Meeting, Vol. 2, ed. L. N. Mavridis, Springer (1974)
 Wilson O. C., Coffeen M. F., Ap. J. 119, 197 (1954)
 Wilson C. P., AJ 80, 175 (1975)

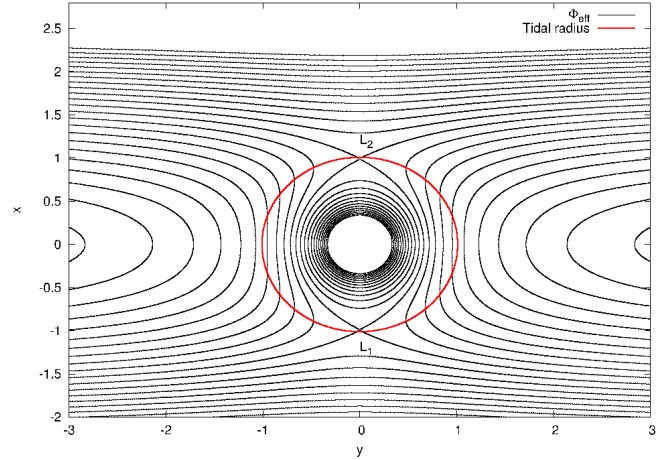


Figure A1. Equipotential lines in the $z=0$ plane for the effective potential (A1) in the case $\kappa^2 \simeq 1.8\omega_0^2$, $\omega_0 = G = 1$. For the star cluster we assumed a Plummer potential, for which we defined a “concentration” $c = \log_{10}(r_t/r_{Pl}) = 1$ and a total mass $M \simeq 2.2$. In these units, we have $r_t = 1$ for the tidal radius and $C_L \simeq -3.3$ for the critical Jacobi integral.

APPENDIX A: THE TIDAL APPROXIMATION

The mean eccentricity of the known 3D globular cluster orbits in the halo of the Milky Way is rather high, see, e.g., Dinescu et al. (1999) or Allen et al. (2006) for a more recent work. Therefore, a realistic tidal field acting on a globular cluster in the Galactic halo should be time-dependant. However, in NBODY6 and NBODY6++, the star cluster is assumed to move around the Galactic center on a circular orbit, which makes it possible to use the epicyclic approximation, cf. Binney & Tremaine (1987). The corresponding tidal field is steady. Its implementation in the N -body code is as follows: As in the restricted three-body problem, one applies a coordinate transformation to a rotating coordinate system with the angular velocity ω_0 , in which both the star cluster center and the Galactic center (i.e., the primaries) are at rest. Its origin is the star cluster center, sitting in the minimum of the effective Galactic potential. The x -axis points away from the Galactic center. The y -axis points in the direction of the rotation of the star cluster around the Galactic center. The z -axis lies perpendicular to the orbital plane and points towards the Galactic North pole. Through this transformation into a frame of reference, in which the tidal potential is static, centrifugal and Coriolis forces appear according to classical mechanics. In addition, tidal terms enter the modified equations of motion in the star cluster region. These can be derived from an effective potential in the epicyclic approximation:

$$\begin{aligned} \Phi_{\text{eff}}(x, y, z) = & \Phi_{\text{cl}}(x, y, z) + \frac{1}{2}\mu^2 x^2 + \frac{1}{2}\nu^2 z^2 \\ & + \mathcal{O}(xz^2) + \text{const} \end{aligned} \quad (\text{A1})$$

where the coordinates are relative to the star cluster center and Φ_{cl} is the star cluster potential. Since the expansion is about the minimum of Φ_{eff} , where the first partial derivatives vanish, there are no first-degree terms in the Taylor expansion. The term $\propto xz$ vanishes because Φ_{eff} is symmetric in z . The term $\propto x^2$ arises from a combination of centrifugal

Isolated system	Tidally limited system
1. $E_\star > 0$	1. $C_\star > C_L$
2. $ \vec{r}_\star - \vec{r}_d > r_{\text{crit}} = 20 \cdot r_V$	2. $ \vec{r}_\star - \vec{r}_d > 2 \cdot r_t$

Table B1. Escape criteria in NBODY6 and NBODY6++.

and tidal forces. For an illustration using a Plummer potential for the star cluster, see Figure A1, which also shows the location of the effective potential's nearest equilibrium points with respect to the star cluster center, which are covered by the approximation: The Lagrangian points L_1 and L_2 , where $\nabla\Phi_{\text{eff}} = 0$. They are saddle points of the effective potential, i.e. the Hessian is neither positive nor negative definite. In terms of Oort's constants A and B , we have in the solar neighborhood

$$\vec{\omega}_0 = (0, 0, \omega_0) = (0, 0, A - B), \quad (\text{A2})$$

$$\kappa^2 = -4B(A - B), \quad (\text{A3})$$

$$\mu^2 = \kappa^2 - 4\omega_0^2 = -4A(A - B) < 0, \quad (\text{A4})$$

$$\nu^2 = 4\pi G\rho_g + 2(A^2 - B^2) > 0, \quad (\text{A5})$$

where κ and ν are the epicyclic and vertical frequencies, respectively. The ratio $\kappa^2/\omega_0^2 \simeq 1.8$ calculated from Oort's constants depends in the general case on the density profile of the Galaxy. The vertical frequency ν can be derived from the Poisson equation for an axisymmetric system, see Oort (1965), and ρ_g is the local Galactic density, which contributes to the dominant first term in (A5).⁵ The equations of motion in the rotating reference frame are then

$$\ddot{\vec{x}} = -\nabla\Phi_{\text{eff}} - 2(\vec{\omega}_0 \times \dot{\vec{x}}), \quad (\text{A6})$$

where the last term on the right-hand side represents the Coriolis forces, which cannot be derived as the usual gradient of a potential, since they are velocity-dependant. After a little bit of vector analysis, the equations of motion read

$$\ddot{x} = f_x + 2(A - B)\dot{y} + 4A(A - B)x \quad (\text{A7})$$

$$\ddot{y} = f_y - 2(A - B)\dot{x} \quad (\text{A8})$$

$$\ddot{z} = f_z - [4\pi G\rho_g + 2(A^2 - B^2)]z, \quad (\text{A9})$$

where $(f_x, f_y, f_z) = -\nabla\Phi_{\text{cl}}$ is the force vector from the other cluster member stars.

APPENDIX B: ESCAPE CRITERIA

In NBODY6 and NBODY6++, the escape criteria shown in Table B1 are implemented. E_\star is the energy of a star, C_\star its Jacobi integral, \vec{r}_\star its position vector, \vec{r}_d the position of the star cluster's density center and r_V is the virial radius. In both the isolated and tidally limited cases, there are a necessary and a sufficient criterion for escape implemented in NBODY6 and NBODY6++. Since the sufficient criterion is always related to a critical radius, we refer to these escape criteria as *radius cutoffs*.

⁵ Actually, such a treatment is only valid in the solar neighborhood, i.e. in the Galactic disk.

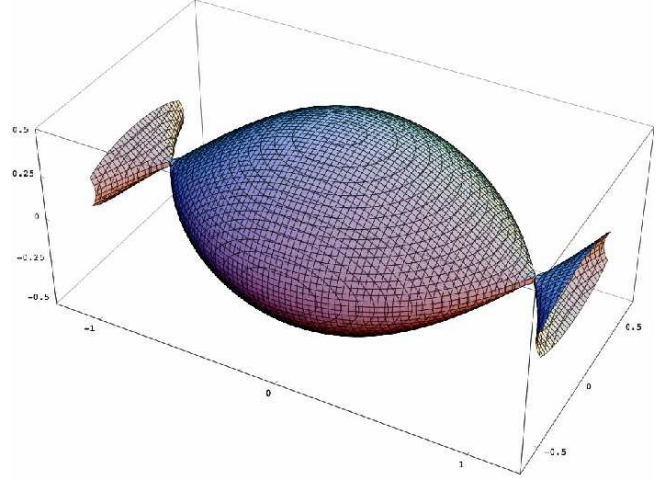


Figure B1. The critical equipotential surface at $\Phi_{\text{eff}} = C_L$ with the same conditions as in Figure A1. We additionally assumed $\nu^2 \simeq 8.5\omega_0^2$. The z -axis is pointing upwards.

The tidal radius is given by

$$r_t = \left[\frac{GM}{4A(A - B)} \right]^{1/3} = \left(\frac{M}{3M_g} \right)^{1/3} R_0 \quad (\text{B1})$$

according to King (1962), where G is the gravitational constant, M is the total mass of the star cluster, A and B are Oort's constants M_g is the mass of the Galaxy and R_0 is the Galactocentric radius of the star cluster's orbit around the Galactic center. The critical Jacobi integral is given by the value of the effective potential (A1) at the Lagrangian points L_1 and L_2 ,

$$C_L = -\frac{3GM}{2r_t} = -\frac{3}{2} [G^2 M^2 4A(A - B)]^{1/3} \quad (\text{B2})$$

according to Wielen (1972). It is conserved in the rotating reference frame, which is centered on the star cluster center. For $C_\star > C_L$, the equipotential surfaces in Figure A1 are open and form channels of escape, through which orbits can leak out. The last closed surface is almond-shaped (see Figure B1).

Takahashi & Portegies Zwart (1998) note that “In an isotropic Fokker-Planck model, one has no choice but to use the energy as a criterion for escape.” What they refer to is the so-called *energy cutoff* in contrast to the *radius cutoff* of the N -body codes. Stars with

$$E > E_t = \Phi(r_t) = -\frac{GM}{r_t} \quad (\text{B3})$$

are removed from the system, where E_t is the tidal energy, i.e. the potential at the tidal radius. This criterion has already been used by Chernoff & Weinberg (1990). Stars, whose energy exceeds the tidal energy by a small amount, are able to cross the tidal radius (if they are on radial orbits). In the energy cutoff picture within the FP approximation, the lifetime of a star cluster scales exactly with relaxation time. However, such an approach may simplify the physics: Once the star's energy is higher than the tidal energy it is called a “potential escaper”: It has not yet escaped but still

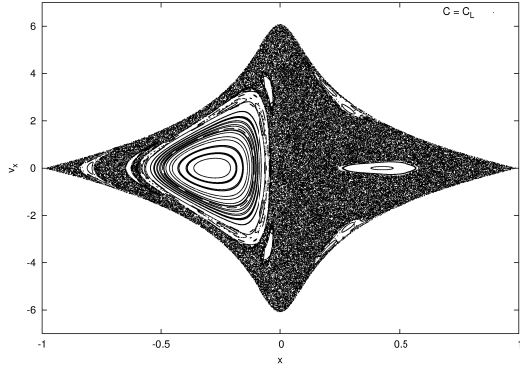


Figure B2. Poincaré section of orbits at the critical Jacobi integral C_L for the equations of motion (A7)-(A8) with the same conditions as in Figure A1 at the moment of crossing $y = 0$ with $\dot{y} > 0$. The full range of initial conditions is covered.

needs a time of the order of the crossing time to reach the tidal radius. Immediate removal of stars which fulfill the energy criterion is only reasonable if the orbital timescale is negligible compared with the relaxation time. An improved approach, which take this dependance on the crossing time scale into account, can be found in the paper by Lee & Ostriker (1987).

In an anisotropic FP code, it is possible to use the more realistic apocentre criterion by Takahashi et al. (1997) and Takahashi & Portegies Zwart (1998): Stars are removed from the system, if their apocenter distance r_a calculated according to

$$J^2 = 2r_a^2 [E - \Phi(r_a)], \quad (\text{B4})$$

exceeds the tidal radius.

Last but not least, in the case of a radius cutoff and the tidal approximation, the picture is similar to the one sketched above: Once a star's Jacobi integral C_* has exceeded the critical value C_L slightly (i.e. once the star is a “potential escaper”), it still needs a certain time to find an opening to one of the escape channels in the equipotential surfaces shown in Figure A1 for the effective potential (A1). This can take many crossing times depending mainly on the excess energy, i.e. we have $t_e \propto C_L^2 (C_* - C_L)^{-2}$ from an upper limit on the flux of phase space volume through L_1/L_2 according to MacKay (1990) and Fukushima & Heggie (2000). In the radius cutoff picture within the tidal approximation, the scaling of the lifetime is very subtle and the half-mass time scales as $t_{\text{mh}} \propto t_{rh}^{3/4}$, see Baumgardt (2001).

By integrating the equations of motion (A7) - (A9) numerically for orbits at a given Jacobi constant, one can obtain a Poincaré section as shown in Figure B2. As seen in this Figure, this is a system with divided phase space: Several “islands” of closed invariant curves in a stochastic “sea” show the existence of an additional conserved quantity other than the Jacobian for these orbits. The largest island of quasiperiodic orbits in the left half of the surface of section corresponds to retrograde orbits, i.e. the stars move around the star cluster in the opposite sense to the motion of the star

cluster around the galaxy, see Fukushima & Heggie (2000). The “third integral” restricts their accessible phase space and hinders them from escaping, even if the stars have been scattered above the critical Jacobi constant. On the other hand, the particles on orbits corresponding to the chaotic domains in the surface of section bounce back and forth for a certain time in a bounded area, called the “scattering region”, until they escape through one of the exits, which open up around the Lagrangian points L_1 and L_2 , for stars with a Jacobi constant, which is higher than the critical value. For an interesting overview of the physics of chaotic scattering see the papers by Aguirre et al. (2001) and Aguirre & Sanjuán (2003).

This paper has been typeset from a $\text{\TeX}/\text{\LaTeX}$ file prepared by the author.